Combustion and Flame 249 (2023) 112622

Contents lists available at ScienceDirect

Combustion and Flame

journal homepage: www.elsevier.com/locate/combustflame

Spark-ignited kernel dynamics in fine ethanol sprays and their relations with minimum ignition energy

Qiang Li, Huangwei Zhang*

Department of Mechanical Engineering, National University of Singapore, 9 Engineering Drive 1, Singapore 117576, Republic of Singapore

ARTICLE INFO

Article history:
Received 17 September 2022
Revised 4 January 2023
Accepted 4 January 2023

Keywords:
Spark ignition
Ethanol
Spray flame
Minimum ignition energy
Equivalence ratio

ABSTRACT

Spark ignition of ethanol droplet/vapor/air mixture is studied with a Eulerian-Eulerian method and detailed chemical mechanism. The flame kernel-droplet interaction is quantified with an evaporation completion front (ECF). Two categories of spray flames can hence be defined based on the relative location between the ECF and flame front, i.e., homogeneous and heterogeneous spray flames. An element-based equivalence ratio (ER) at the flame front (flame ER for short) is introduced to measure the gas composition in evaporating sprays. For overall fuel-lean mixtures, quasi-stationary spherical flame (QSSF) occurs due to lean flame ER and the composition at the QSSF front is homogeneous. For overall fuel-rich two-phase mixtures, re-ignition, after the spark-ignited kernel fails, is observed when the droplet diameter is 15 μm for fuel sprays with both fuel-lean and fuel-rich background gas. This is due to rich flame ER and/or strong evaporative heat loss. Meanwhile, the kernel is born in a heterogeneous mixture and transition into homogeneous state is found. For both overall lean and rich two-phase mixtures, fuel droplets affect the ignitability and flame trajectories. Moreover, ignition energy affects the flame ER and front distance at the early stage of kernel development. Lastly, the minimum ignition energies (MIE) with different gas and overall ERs are investigated. Three regimes (A, B and C) are identified from the MIE variations with overall ER and the corresponding flame kernel dynamics behind them are summarized. Regime A is characterized by the QSSF phenomenon, whilst regime C embodies the ignition failure and re-ignition transients when the droplet size is relatively large. Furthermore, regime B only appears with a narrow range of overall ER when initial background gas ER is above unity. These regimes are further generalized in parameter space of overall ER versus initial background gas ER.

1. Introduction

Flame–droplet interaction in spray combustion is a critical topic in both fundamental combustion theory and applied combustion study [1–3]. Due to existence of the dispersed fuel droplets, spray flames exhibit peculiar structures and/or dynamic behaviors different from gaseous flames. For instance, Mizutani et al. [4] and Akamatsu et al. [5] observed a two-layer structure, consisting of a nonluminous flame front and luminous flamelets behind the flame front. The latter is caused by post-flame droplet burning. The two-layer spray flame structure is also observed by Fan et al. [6] when acetone droplets are added to the methane/air mixture. According to the direct numerical simulations by Neophytou et al. [7], a triple flame is observed, which results from the high-concentration fuel vapor from droplet evaporation around the spark. Moreover, flame wrinkling induced by droplet evaporation near the flame front is reported by Ozel et al. [8]. Three distinctive modes of spray flame propagation are identified by de Oliveira and Mastorakos [9] with schlieren and OH* chemiluminescence methods, including droplet, inter-droplet and gaseous-like modes. Flame wrinkling and droplet penetration to the post-flame zone occur in the first two modes with a small Group combustion number ($< 10^2$). Recently, Li and Zhang [10] find quasi-stationary flame kernel and failure/re-ignition transient in spark ignition of ethanol sprays. They also conclude that these two phenomena are related to heat and mass exchange from droplet evaporation.

Interactions between the flame front and evaporating sprays are directly influenced by their spatial distributions. Generally, two scenarios exist [9,11–16]: (I) fuel droplets only exist in the pre-flame zone; (II) fuel droplets exist in both pre- and post-flame zones. In scenario I, the droplets are fully vaporized before the flame front, whereas in scenario II the droplets cannot complete the evaporation in the pre-flame zone and hence penetrate through the flame front. Their occurrence is influenced by droplet properties. For instance, scenario I is observed for relatively fine droplets (acetone: 5 μm [6]; *iso*-octane: 10 μm [17]), whereas sce-

* Corresponding author.
E-mail address: huangwei.zhang@nus.edu.sg (H. Zhang).

https://doi.org/10.1016/j.combustflame.2023.112622
0010-2180/

Nomenclature

A_d	surface area of a single droplet [m^2]
AF_s	molecular ratio of air/fuel under stoichiometric condition for gas mixture
a_i	constants related to fuel saturation pressure
B_M	mass transfer number
B_T	heat transfer number
b_i	constants related to the latent heat of vaporization
C_d	drag coefficient
$C_{p,d}$	heat capacity at constant pressure for fuel droplet [J/kg/K]
$C_{p,v}$	heat capacity at constant pressure for fuel vapor [J/kg/K]
D_{ab}	vapour mass diffusivity in the gas phase [m^2/s]
d	droplet diameter [m]
E	total energy of gas phase [J/m^3]
E_{ig}	ignition energy [J]
F_s	drag force [N]
HRR	heat release rate [W/m^3]
$H_g(T_d)$	enthalpy of ethanol vapor at the droplet temperature [J/kg]
h	total enthalpy of gas [J/kg]
h_c	convective heat transfer coefficient [$W/m^2/K$]
k_g	thermal conductivity of gas [W/m/K]
Le	Lewis number of gas phase
$L_v(T_d)$	latent heat of vaporization at the droplet temperature [J/kg]
M_d	molecular weight of droplet [kg/mol]
M_{ed}	mean molecular weight of the gas mixture excluding the fuel vapor [kg/mol]
M_g	molecular weight of gas mixture [kg/mol]
$\dot{m}$	evaporation rate of a single droplet [kg/s]
m_d	mass of a single droplet [kg]
N_d	number density of droplet [m^{-3}]
N_u	Nusselt number
n	total number of species
Pr	Prandtl number
p_g	gas pressure [Pa]
p_f	partial pressure for fuel vapor in the gas mixture [Pa]
p_s	fuel vapor pressure at droplet surface [Pa]
p_{sat}	saturation pressure for fuel vapor [Pa]
q_{ig}	ignition energy source term [W/m^3]
R	universal gas constant [J/mol/K]
R_{ed}	droplet Reynolds number
R_c	evaporation completion front [m]
R_f	flame front [m]
r	radial coordinate [m]
r_{ig}	spark radius [m]
r_w	computational domain length [cm]
Sc	Sherwood number
S_b	flame propagation speed [m/s]
Sh	Schmidt number
S_I	ignition source term
S_L	liquid phase source term
S_R	chemical reaction source term [$kg/m^3/s$] or [$kg/m^2/s^2$] or [W/m^3]
S_e	energy exchange source term [W/m^3]
$S_{m,i}$	mass exchange source term for i-th species [$kg/m^3/s$]
S_v	momentum exchange source term [$kg/m^2/s^2$]
T_{cr}	critical temperature of fuel [K]
T_d	droplet temperature [K]
T_r	temperature ratio, defined as T_d/T_{cr}
T_s	vapor temperature at the droplet surface [K]
T_{sat}	saturation temperature [K]
t	temporal coordinate [s]
U	conservative variables
u_d	droplet velocity [m/s]
u_g	gas velocity [m/s]
V_i'	diffusion velocity of i th species [m/s]
V_1, V_2	constants related to the fuel vapor mass diffusivity
X_C	local element mole fraction of C
X_{ds}	ethanol vapor mole fraction at the droplet surface
X_H	local mole fraction of H element
X_O	local mole fraction of O element
Y_{ds}	ethanol vapor mass fraction at the droplet surface
$Y_{d\infty}$	ethanol vapor mass fraction in the bulk gas
Y_i	mass fraction of i th species in gas mixture

Greek letters

ΔR	difference between evaporation completion front and flame front [m]
ρ_d	density of fuel droplet [kg/m^3]
ρ_g	density of gas mixture [kg/m^3]
ρ_s	density of fuel vapor at the droplet surface [kg/m^3]
Φ	viscous dissipation rate of energy [W/m^3]
ϕ_e	effective equivalence ratio
ϕ_g	equivalence ratio of gas mixture
ϕ_l	liquid fuel equivalence ratio
ϕ_{ov}	overall equivalence ratio
τ_1, τ_2	viscous stress [Pa]
τ_{ig}	spark duration time [m]
τ_r	droplet momentum relaxation time [s]
μ_g	Dynamic viscosity of gas [Pa·s]
ω_i	chemical reaction rate for i th species [$kg/m^3/s$]

Subscripts

d	properties related to droplet
g	properties related to gas
f	properties related to flame front
s	properties related to droplet surface
0	properties related to initial state

nario II occurs for coarse droplets (acetone: 65 – 75 μm [18]). Moreover, both scenarios are found in Jet-A spray flame with varied droplet sizes (16 – 33 μm) [9,19]. They typically result in different spray flame behaviors. For instance, flame front cellularization only occurs in scenario II according to Thimothée et al. [20]. Meanwhile, flame speed oscillation is correlated with the periodical transition between scenario I and II [15]. Most of the foregoing studies target spray flame propagation. Recently, to capture the intrinsic evolutions of two scenarios in a spray ignition process, Li et al. [14] develop a theoretical model through introducing the concepts of evaporation onset and completion fronts, and hence the interactions between the flame front and the above two can be quantified. The results show that the igniting kernel transits from scenario II to I and change of the distributions of droplets relative to the reaction front leads to different kernel evolutions. Nonetheless, due to the limitations of theoretical analysis, how the two scenarios evolve under various spray conditions is not analyzed therein, which merits further studies with detailed numerical simulation and/or high-resolution experimental measurements.

There have been a large body of investigations on minimum ignition energy (MIE) of spray flames. The experiments by Rao and Lefebvre [21], Ballal and Lefebvre [22–25], and Danis et al. [26] show that the MIE monotonically increases with droplet diameter when the latter is relatively large, i.e., > 30 μm. For smaller

droplets, the MIE increases with decreased diameter [2,27]. Therefore, there exists an optimal diameter corresponding to the smallest MIE, e.g., around 25 μm for overall fuel-lean *n*-heptane spray flames [26]. Moreover, the mixture composition, parameterized by gas (ϕ_g) and liquid (ϕ_l) equivalence ratios, also affects the MIE. For instance, for pure sprays ($\phi_g = 0$), the MIE monotonically decreases with ϕ_l for kerosene [21–23], isooctane [24,25] and *n*-heptane [26] sprays with fixed droplet size. However, other researchers have reported the existence of an optimal ϕ_l in their studies, corresponding to the smallest MIE [28–30]. Furthermore, for partially pre-vaporized sprays ($\phi_g \neq 0$), the gas phase equivalence ratio, ϕ_g, also influences the MIE [31,32]. Nonetheless, the intrinsic relations between MIE variation and flame kernel dynamics in fuel sprays have not been correlated in previous studies.

Based on the above consideration, we aim to study spark ignition of ethanol droplet/vapor/air mixtures with detailed chemistry. The influences of gas phase and liquid phase properties will be examined, including droplet diameter, gas, and liquid equivalence ratios. The objectives of this work include: (1) flame kernel development in fuel sprays and comparison with gaseous flames; (2) flame kernel-droplet interactions; and (3) correlation between flame kernel development modes and MIE variations. The rest of the paper is structured as below. The mathematical model is presented in Section 2, whilst the physical model and numerical implementations are listed in Section 3. The results will be discussed in Section 4, followed by the key conclusions in Section 5.

2. Mathematical model

Spark ignition of two-phase ethanol droplet/vapor/air mixtures is simulated with Eulerian–Eulerian method. An in-house reactive flow solver with detailed chemistry and species transport properties, A-SURF [33,34], is used. The accuracies of A-SURF in simulating both gaseous and spray flames have been validated in previous studies [10,34,35]. The governing equations and models are presented below.

2.1. Gas phase

The equations for multi-species reactive flows in one-dimensional spherical coordinate read

$$\frac{\partial U}{\partial t} + \frac{\partial F(U)}{\partial r} + 2\frac{G(U)}{r} = F_v(U) + S_R + S_L + S_I \ . \tag{1}$$

Here t and r are time and radial coordinates, respectively. The vector U is the conservative variables, whilst $\partial F(U)/\partial r$, $2G(U)/r$, and $F_v(U)$ are the convection, geometry, and diffusion terms, respectively. S_R and S_I denote chemistry and numerical spark terms, respectively. Detailed descriptions for U, $F(U)$, $G(U)$, $F_v(U)$ and S_R in Eq. (1) can be found in previous studies [33,34]. The effects of fuel droplets on the gas phase are considered through the source/sink terms S_L, i.e.,

$$S_L = [S_{m,1}, S_{m2,} \ldots, S_{m,i}, \ldots, S_{m,n}, S_v, S_e]^T. \tag{2}$$

In Eq. (2), S_L includes the species ($S_{m,i}$), momentum (S_v) and energy (S_e) transfer terms. They are

$$S_{m,i} = \begin{cases} N_d\dot{m} & for\ ethanol \\ 0 & for\ other\ species \end{cases}, \tag{3}$$

$$S_v = -N_d m_d \frac{u_g - u_d}{\tau_r}, \tag{4}$$

$$S_e = -N_d h_c A_d (T_g - T_d) + N_d \dot{m} H_g(T_d). \tag{5}$$

Here $H_g(T_d)$ is the enthalpy of ethanol vapor at the droplet temperature, N_d is the number density of the fuel droplet. $\dot{m}$ is the evaporation rate of a single droplet, whilst m_d is the mass of a single droplet. u_d and T_d are the droplet velocity and temperature, respectively. τ_r is droplet momentum relaxation time. h_c is the convective heat transfer coefficient. A_d is the surface area of a single droplet as $A_d = \pi d^2$, where d is the droplet diameter.

2.2. Liquid phase

The Eulerian approach is applied to describe the dispersed spray droplets, and equations of droplet size, velocity, temperature, and number density are solved. Note that mono-sectional method is employed and therefore all the droplets of the relevant sprays are represented by one section. Spherical droplets are considered, and droplet temperature is assumed to be uniform due to their small Biot number [36,37]. Moreover, droplet breakup and/or deformation are not considered due to fine droplets and weak aerodynamic fragmentation effects.

The evolution of droplet diameter, d, is governed by

$$\frac{\partial d}{\partial t} + u_d \frac{\partial d}{\partial r} = -\frac{2\dot{m}}{\pi \rho_d d^2}, \tag{6}$$

where ρ_d is droplet material density, taking 783.54 kg/m^3 for ethanol. The droplet evaporation rate $\dot{m}$ is modeled as [38]

$$\dot{m} = \pi d \rho_s D_{ab} Sh \ln(1 + B_M), \tag{7}$$

where $\rho_s = p_s M_d / R T_s$ is the vapor density at the droplet surface. p_s and T_s are the vapor pressure and temperature at the droplet surface, respectively. M_d is the molecular weight of ethanol vapor. T_s is estimated through $T_s = (2T_d + T_g)/3$ [38], in which T_g is the gas temperature.

The Spalding mass transfer number B_M is

$$B_M = \frac{Y_{ds} - Y_{d\infty}}{1 - Y_{ds}}, \tag{8}$$

where $Y_{d\infty}$ is the ethanol vapor mass fraction in the bulk gas. Y_{ds} is the ethanol vapor mass fraction at the droplet surface, i.e.,

$$Y_{ds} = \frac{M_d X_{ds}}{M_d X_{ds} + M_{ed}(1 - X_{ds})}. \tag{9}$$

Here M_{ed} is the mean molecular weight of the gas mixture excluding the ethanol vapor. X_{ds} is the ethanol vapor mole fraction at the droplet surface

$$X_{ds} = \frac{p_{sat}(T_d)}{p_g}, \tag{10}$$

where p_g is the pressure for gas mixture. p_{sat} is the saturated vapor pressure and is estimated as a function of droplet temperature T_d [39]

$$p_{sat}(T_d) = exp\left(a_1 + \frac{a_2}{T_d} + a_3 \ln T_d + a_4 T_d^{a_5}\right). \tag{11}$$

The constants a_1, a_2, a_3, a_4, and a_5 are 59.769, −6595.0, −5.0474, 6.3 $\times 10^{-7}$ and 2.0, respectively [39]. Similarly, the vapor pressure at the droplet surface p_s is estimated with the droplet surface temperature T_s, i.e.,

$$p_s(T_s) = exp\left(a_1 + \frac{a_2}{T_s} + a_3 \ln T_s + a_4 T_s^{a_5}\right). \tag{12}$$

Moreover, in Eq. (8), the vapor mass diffusivity in the gas mixture, D_{ab}, is modeled as [40]

$$D_{ab} = 3.6059 \times 10^{-3} \frac{(1.8 \times T_s)^{1.75}}{p_g} \times \sqrt{\frac{1}{M_d \times 10^3} + \frac{1}{M_g \times 10^3}} \Big/ \left(V_1^{\frac{1}{3}} + V_2^{\frac{1}{3}}\right)^2. \tag{13}$$

The constants V_1 and V_2 are 141.78 and 20.1 respectively for ethanol and air mixture [41].

The Sherwood number Sh in Eq. (7) is estimated from [38]

$$Sh = 2.0 + \frac{1}{f(B_M)}\left[(1 + Re_d Sc)^{1/3}\max(1, Re_d)^{0.077} - 1\right]. \quad (14)$$

In the above, $f(B) = \ln(1+B)/B \cdot (1+B)^{0.7}$ is used to model the change of film thickness due to Stefan flow effects [38]. The Schmidt number Sc of the gas phase is

$$Sc = \frac{\mu_g}{\rho_g D_{ab}}. \quad (15)$$

In Eq. (14), the droplet Reynolds number Re_d is defined as

$$Re_d \equiv \frac{\rho_g d|u_g - u_d|}{\mu_g}, \quad (16)$$

where μ_g is the dynamic viscosity of the gas mixture.

The equation of droplet velocity takes the following form

$$\frac{\partial u_d}{\partial t} + u_d \frac{\partial u_d}{\partial r} = \frac{F_s}{m_d}. \quad (17)$$

Note that only drag force F_s is considered in our work and it is modelled from $F_s = m_d/\tau_r \cdot (u_g - u_d)$, where $m_d = \rho_d \pi d^3/6$. τ_r is determined from [42]

$$\tau_r = \frac{\rho_d d^2}{18\mu_g}\frac{24}{C_d Re_d}. \quad (18)$$

The drag coefficient C_d is modelled as [42]

$$C_d = \begin{cases} \frac{24}{Re_d}\left(1 + \frac{1}{6}Re_d^{2/3}\right), & if\ Re_d \le 1000 \\ 0.424, & if\ Re_d > 1000 \end{cases}. \quad (19)$$

Evolution of the droplet temperature is governed by

$$m_d C_{P,d}\left(\frac{\partial T_d}{\partial t} + u_d \frac{\partial T_d}{\partial r}\right) = h_c A_d (T_g - T_d) - \dot{m} L_v(T_d), \quad (20)$$

where $C_{P,d}$ is the specific heat capacity of the liquid ethanol. $L_v(T_d)$ is the latent heat of vaporization at the droplet temperature and estimated from [43]

$$L_v(T_d) = b_1 \cdot (1 - T_r)^{[(b_2 \cdot T_r + b_3)\cdot T_r + b_4]\cdot T_r + b_5}, \quad (21)$$

where the constants b_1, b_2, b_3, b_4, and b_5 are 958,345.09 J/kg, -0.4134, 0.75362, 0, and 0 respectively for liquid ethanol [43]. T_r is defined as $T_r = T_d/T_{cr}$, where T_{cr} is the critical temperature and is 516.25 K for ethanol.

In Eq. (20), the convective heat transfer coefficient h_c is

$$h_c = \frac{Nuk_g}{d}, \quad (22)$$

where k_g is the thermal conductivity of the gas mixture. Nu is the Nusselt number, estimated with Rans and Marshall model [44]

$$Nu = 2.0 + \frac{1}{f(B_T)}\left[(1 + Re_d Pr)^{1/3}\max(1, Re_d)^{0.077} - 1\right], \quad (23)$$

where Pr is the Prandtl number of the gas phase and assumed to be unity in this study. $B_T = (1+B_M)^{\varphi} - 1$ is the Spalding heat transfer number, in which $\varphi = (C_{p,v}/C_{P,d})/Le$. Le is the Lewis number of the gas mixture and $C_{p,v}$ is the constant pressure specific heat of ethanol vapor.

The equation of droplet number density N_d reads

$$\frac{\partial N_d}{\partial t} + \frac{\partial (N_d u_d)}{\partial r} + 2\frac{N_d u_d}{r} = 0. \quad (24)$$

3. Physical model description and characterization

Spark ignition in fine ethanol sprays is simulated with a one-dimensional configuration. The computational domain length is $0 \le r \le r_w$, in which r_w is 20.48 cm. Adaptive mesh refinement is used to accurately capture the reactive front and droplet evaporation front with relatively low cost. A refinement level of 8 is used, leading to the finest cell size of 16 μm, which can accurately capture the flame front. Moreover, in this work, the initial droplet diameter, d_0, ranges from 5 to 15 μm. With this diameter range, we test various cell sizes and find that the droplet evaporation rate is almost not affected.

Operator splitting approach is applied to sequentially calculate the chemistry and convection/diffusion terms. The time integration, diffusive flux, convective flux, and liquid properties (T_d, u_d, d and N_d) are calculated by the second-order Runge-Kutta, second-order central differencing, MUSCL-Hancock, and first-order upwind schemes [45], respectively. A detailed mechanism (57 species and 383 reactions) [46] is considered for ethanol combustion, which has also been used in previous studies for ethanol spray flames [47–49].

The initial gas flow velocity is zero, i.e., $u_{g,0} = 0$ m/s. The domain is initially filled with a heterogeneous mixture of ethanol droplets, vapor, and air. The reaction system is characterized by liquid fuel and gaseous vapor Equivalence Ratios (ER), i.e., ϕ_g and ϕ_l. The overall ER can be calculated from $\phi_{ov} = \phi_g + \phi_l$. In our simulations, ϕ_g ranges from 0.3 to 2.0, while ϕ_{ov} is from 0.8 to 4.0. The values of ϕ_g/ϕ_{ov} and ϕ_l are selected to cover overall fuel-lean to overall fuel-rich conditions. The initial pressure is $p_{g,0} = 1$ atm. The initial gas temperature, $T_{g,0}$, is assumed to be the saturation temperature T_{sat}, with which the partial pressure of pre-vaporized ethanol vapor in a gas mixture with a specific equivalence ratio ϕ_g is equal to the corresponding saturation vapor pressure of $p_{sat}(T_{sat})$. This ensures that the evaporation of ethanol droplets before the flame front is inhibited, and therefore the vapor release is fully caused by the flame–droplet interactions. The partial pressure of the ethanol vapor, $p_{0,f}$, before sparking is

$$p_{0,f} = \frac{\phi_g}{\phi_g + AF_s} p_{g,0}, \quad (25)$$

where AF_s is the air/fuel molar ratio for a stoichiometric gas mixture, which is approximately 14.28 for ethanol/air mixture. For ϕ_g studied in this paper (0.3–2.0), the fuel partial pressure $p_{0,f}$ varies from 0.02 to 0.123 atm, whilst the resultant T_{sat} (hence $T_{g,0}$) ranges from 277.8 to 310.4 K. Such small temperature differences are expected to have negligible effects on kernel development.

Before ignition, the fuel droplets are static ($u_{d,0} = 0$) and uniformly distributed in the domain. The initial droplet temperature, $T_{d,0}$, is the same as the gas temperature. Moreover, the initial number density of the fuel droplets, $N_{d,0}$, can be estimated from [50]

$$N_{d,0} = \frac{\phi_l}{\phi_g + AF_s}\frac{p_{g,0} M_d}{R T_{g,0}} / \left(\pi \rho_d d_0^3/6\right). \quad (26)$$

For the initial conditions considered in this study, $N_{d,0}$ ranges from approximately 8400 to 9320,000 cm^{-3}. The resultant droplet numbers in the finest cell are above 1000. As such, the Eulerian description for the liquid phase is generally valid. Details of the estimations can be found in Fig. S1 from Supplemental Material.

Zero-gradient conditions for species mass fractions, temperature, and liquid phase variables (diameter, temperature, and number density) are enforced at both spherical center ($r = 0$) and right boundary ($r = r_w$). Zero velocities of the gas and droplets are applied for two boundaries. To mimic the energy deposition from a spark, a source term is added for the gas phase energy equation

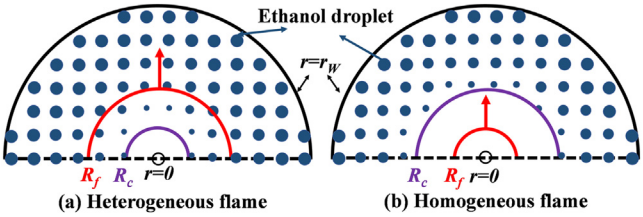

Fig. 1. Schematic of (a) heterogeneous and (b) homogeneous spray flames. Red arrow indicates flame propagates direction. Circles: fuel droplets.

(i.e., S_l in Eq. (1)) [51]

$$q_{ig}(r,t)=\begin{cases}\frac{E_{ig}}{\pi^{1.5}r_{ig}^3\tau_{ig}}\exp\left[-\left(\frac{r}{r_{ig}}\right)^2\right], & if\ t<\tau_{ig}\\ 0, & if\ t\geq\tau_{ig}\end{cases} \quad (27)$$

where E_{ig} is the ignition energy, whilst r_{ig} and τ_{ig} are the spark size and duration, respectively. In this study, $\tau_{ig}=400\ \mu s$ and $r_{ig}=400\ \mu m$ are assumed [52,53].

The interactions between fuel droplets and flame front are critical to spray flame dynamics [13,14,19,54]. Therefore, besides the evaporation fronts proposed in previous theoretical [13,14] and numerical [10] studies, here we further define the evaporation completion front (ECF, R_c). It is the location where the fuel droplets are just fully vaporized (droplet diameter $d\leq 0.1$ μm). For an outwardly propagating spherical spray flame, this indicates that the droplet diameter $d>0.1$ μm when the radial coordinate $r>R_c$. Behind the ECF, i.e., $r\leq R_c$, the droplet diameter $d\leq 0.1$ μm. Further decreasing the diameter threshold would almost not affect the ECF locations (see Fig. S2 in the Supplemental Material).

Besides, the flame front (FF), R_f, is defined as the location with the maximum heat release rate (HRR). If $\Delta R<0$, the ECF is behind the FF. Hence, the mixture at the FF is composed of evaporating droplets and gas. This is deemed a *heterogeneous* (HT) spray flame (Fig. 1a), i.e., Scenario II discussed in Section 1. If the front distance $\Delta R=R_c-R_f<0$, then the ECF lies at the unburned zone, indicating that the mixture at the FF is gaseous. This is termed a *homogeneous* (HM) spray flame (Fig. 1a), corresponding to Scenario I discussed in Section 1. Note that, for one-dimensional simulations, the flame front cellularization, e.g., observed in Ref. [20], cannot be predicted in our studies.

To quantify the evolving gas composition due to evaporating sprays in both HM and HT cases, an element-based effective ER [55] is calculated for the gas phase, i.e.,

$$\phi_e=\left[3\left(\frac{X_C}{2}+\frac{X_H}{6}\right)\right]/\left[X_O-\frac{1}{2}\left(\frac{X_C}{2}+\frac{X_H}{6}\right)\right] \quad (28)$$

where X denotes the mole fraction of an element (i.e., C, H or O). We always quantify the ϕ_e at the FF, $\phi_{e,f}$, and in our following discussion we simply term it as flame ER.

4. Results and discussion

4.1. Flame kernel development in fuel-lean two-phase mixtures

This section will investigate the flame kernel development in overall fuel-lean ethanol droplet/vapor/air mixtures. The selected conditions are $\phi_g=0.5$, $\phi_l=0.3$, and $d_0=5$ μm, which is called case 1. Firstly, Fig. 2(a)–(d) present the *r-t* diagrams of fuel mass fraction Y_F, heat release rate (HRR), magnitude of energy transfer term S_e and mass transfer term $S_{m,F}$ in case 1, respectively. The magnitude of S_e and $S_{m,F}$ are selected to show the location with high evaporation intensity in *r-t* space. Noted that E_{ig} of Fig. 2 is 3.3 mJ (MIE of case 1). The trajectories of FF and ECF are also presented in Fig. 2(a).

The kernel development in case 1 can be divided into three stages based on the evolutions of FF and ECF, which are identified by points A and B in Fig. 2(a). Stage 1 starts from $t=0$ to the point when FF and ECF decouple, i.e., approximate point A (0.18 cm, 0.66 ms). In this stage, both chemical reaction and droplet evaporation are largely driven by energy deposition from the spark. Therefore, the HRR, energy and mass transfer terms before A are considerable, see Fig. 2(b)–(d). In stage 2 (A → B), a quasi-stationary spherical flame (QSSF) is observed. It is seen that the FF displacement is small in stage 2. This results from deficient fuel vapor supply, demonstrated by low Y_F value between FF and ECF in stage 2 (Fig. 2a). The chemical reaction is hence weakened (Fig. 2b). Meanwhile, the evaporation intensities indicated by the magnitudes S_e and $S_{m,F}$ are also reduced. Nonetheless, the ECF continues moving outwardly due to the thermal diffusion from the flame kernel to fuel droplets. This causes a negative gradient of Y_F between the ECF and FF due to droplet evaporation before ECF. Consequently, fuel vapor diffuses from the ECF to FF. Beyond point B, the QSSF kernel is intensified through the continuous fuel vapor supply during the QSSF period. The kernel growth is therefore accelerated, and the period after B corresponds to stage 3. At this stage, the FF accelerates expansion firstly and couples with the ECF again at point C.

To further understand the flame kernel development in case 1, the corresponding evolutions of flame propagation speed ($S_b\equiv dR_f/dt$ and front distance ΔR) are presented in Fig. 3(a). In Fig. 3(b) and 3(c), the flame trajectories and flame ER in case 1 and two gaseous ethanol flames with the ER being 0.5 and 0.8 (respectively corresponding to ϕ_g and ϕ_{ov} in case 1) are compared. The ignition energies of the two gaseous flames equal the MIE of case 1. Compared to Ref. [10], the partial pre-vaporization condition in this study provides the possibility of background gas ignition (gas flame with ϕ_g), besides the reactive sprays. Moreover, the gas ER is also critical to the spray flame kernel growth. Therefore, it is necessary to investigate the difference between the spray case and two corresponding gaseous flames.

In Fig. 3(a), at the beginning of stage 1, the FF and ECF synchronously move outwardly with a small front distance ΔR. Furthermore, the flame transits from heterogeneous ($\Delta R<0$) to homogeneous ($\Delta R>0$) condition. Initially, the flame ER is close to the overall ER of 0.8 (see Fig. 3c). Then, the flame ER gradually decreases in stage 1 due to the kernel decaying after the spark is terminated at t_{ig}. In stage 2, we can see that the flame propagation speed is smallest (≈ 4 cm/s) at point B, which is also the location of maximum ΔR. This indicates the diffusion length for the ethanol vapor to be transported from the evaporation zone to FF is increased and reaches the maximum value at B. Decreased flame ER between A and B is observed (from 0.6 to 0.47), which is even smaller than the lower flammability limit (LFL) of ethanol (about 0.5 [56]), as marked in Fig. 3(c). Beyond point B, it is seen that S_b gradually increases, while ΔR decreases. The flame ER also increases accordingly.

For the two gaseous flames in Fig. 3(b), it is seen that their trajectories are almost identical to case 1 in the sparking period ($t<t_{ig}$). Afterwards, the gaseous flame with $\phi_g=0.8$ (0.5) accelerates (decelerates), leading to successful (failed) ignition event. Compared to the $\phi_g=0.8$ gaseous flame, existence of the fuel droplets in case 1 corresponds to lower ER in the gas phase, see Fig. 3(b). This essentially induces the peculiar QSSF phenomenon in case 1. On the contrary, the ignitibility of the leaner background premixture (i.e., ER = 0.5) is improved due to the addition of fuel droplets compared to the $\phi_g=0.5$ gaseous flame, which is demonstrated by higher flame ER in case 1 as observed from Fig. 3(c).

The ignition energy typically affects the flame kernel trajectory in a spark ignition process [35,53]. This has not been discussed in our previous studies [10]. The flame trajectories of case 1 with dif-

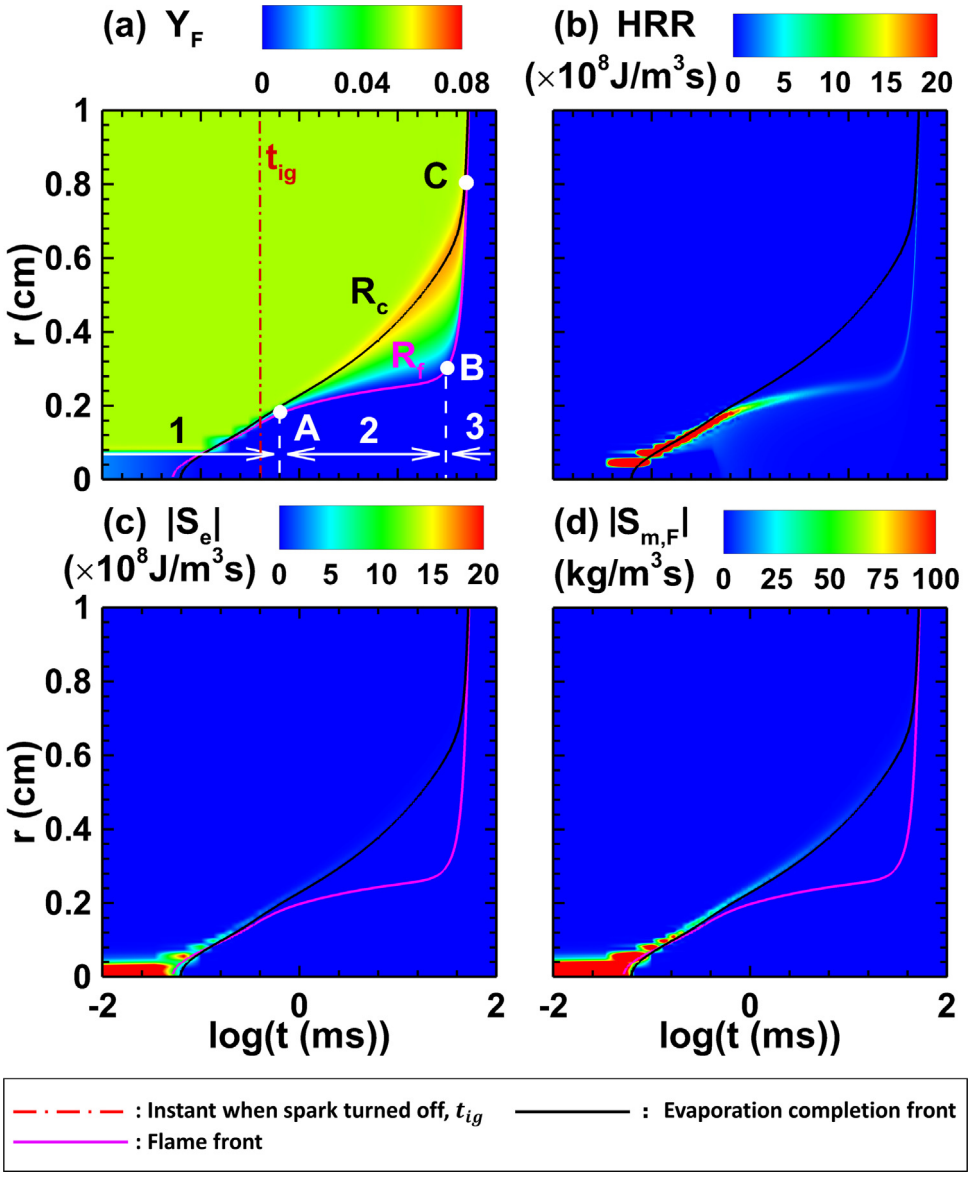

Fig. 2. $r-t$ diagrams of (a) fuel vapor mass fraction, (b) heat release rate, (c) magnitude of energy transfer term and (d) mass transfer term with $\phi_g = 0.5$, $\phi_l = 0.3$, and $d_0 = 5$ μm. $E_{ig} = 3.3$ mJ.

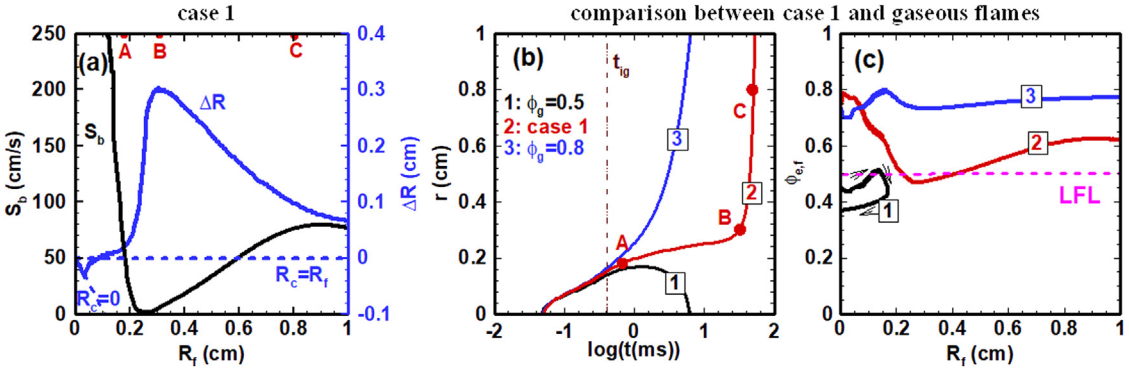

Fig. 3. (a) Change of flame propagation speed and front distance with flame radius in case 1. (b) Flame trajectories and (c) change of flame ER with flame radius in case 1 and two gaseous flames with ER = 0.5 and 0.8. LFL: lower flammability limit. Points A, B and C are the same as in Fig. 2(a). $E_{ig} = 3.3$ mJ.

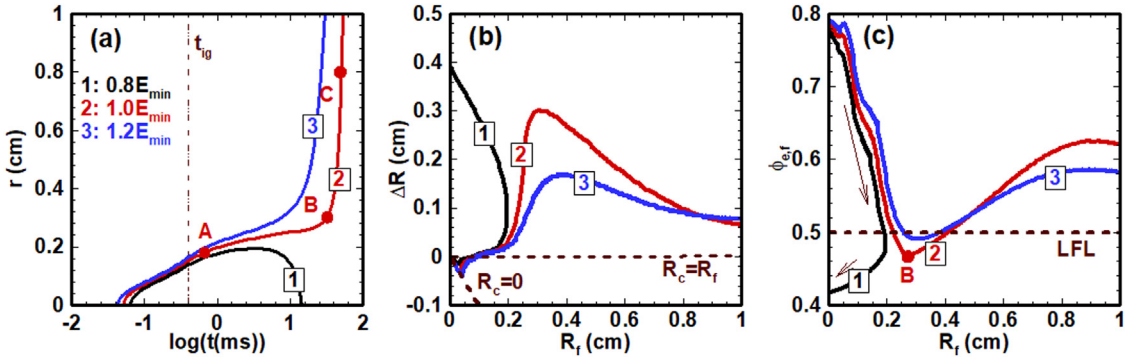

Fig. 4. (a) Flame trajectories of case 1 with different ignition energies. Change of (b) front distance and (c) flame ER in case 1 with different ignition energies. The arrow in (c) indicates kernel propagation direction.

ferent ignition energies are presented in Fig. 4(a). Meanwhile, the evolutions of the front distance and flame ER in case 1 with different ignition energies are presented in Fig. 4(b) and 4(c), respectively. As seen from Fig. 4(a), the flame with $1.2E_{min}$ propagates faster than the MIE condition. The QSSF phenomenon is not as obvious as in case 1 with increased ignition energy. Nonetheless, for the $0.8E_{min}$ flame, ignition failure occurs.

In Fig. 4(b), one can see that at the very early sparking period, the droplets are fully dispersed in the post-flame zone in all ignition events, which is indicated by the dashed line $R_c = 0$. After a finitely long duration, the ECF starts to deviate from the spherical center (i.e., the droplets near the spark have fully vaporized due to their longer exposure to the local hot gas). Subsequently, the kernel transits from the HT to the HM flames. Furthermore, if $E_{ig} < E_{min}$, i.e., line #1, failed ignition occurs. This leads to the shrinkage of the kernel in Fig. 4(b). Meanwhile, the hot kernel continuously vaporizes fuel droplets in the pre-flame zone, resulting in increased ΔR. As for the successful ignition events (line #3), ΔR decreases with flame radius after reaching the maximum value because the flame is intensified after the QSSF period. Meanwhile, the maximum ΔR decreases with increased E_{ig}. The evolutions of the front distance in Fig. 4(a) for both failed and successful ignition events show qualitative accordance with previous theoretical analysis on fuel spray ignition [57].

In Fig. 4(c), increased ignition energy leads to a slightly richer flame ER at the early stage, i.e., $R_f < 0.2$ cm. At this stage, the flame ER of each event decreases as the kernels expand. Beyond this, the flame ER of line #1 further decreases due to increased front distance (increased diffusion length). As for lines #2 and #3, the minimum flame ER (e.g., point B for line #2) increases with increased ignition energy. This is caused by the intensified evaporation process for increased ignition energy. This can be confirmed by the mass transfer terms from three ignition events (see Fig. S3 in the Supplemental Material).

4.2. Flame kernel development in fuel-rich two-phase mixtures

The flame kernel development in overall fuel-rich ($\phi_{ov} > 1.0$) mixtures will be investigated in this section. Fuel-lean ($\phi_g < 1.0$) and fuel-rich background gas ($\phi_g > 1.0$) are considered in Sections 4.2.1 and 4.2.2, respectively.

4.2.1. Fuel-lean background gas ($\phi_g < 1.0$)

The selected conditions are $\phi_g = 0.3$, $\phi_l = 1.7$, and $d_0 = 15$ μm, which is case 2. Here the ignition energy is its MIE (1.76 mJ). Figure 5(a)–(d) show the $r - t$ diagrams of Y_F, HRR, magnitude of energy transfer term and mass transfer term, respectively. Moreover, the fuel / oxidizer mass fractions and effective ER at some milestones, marked by D_1 - F in Fig. 5(a), are shown in Fig. 6.

Four stages can be identified in the flame kernel development from Fig. 5(a). Stage I is the spark ignition stage, from $t = 0$ to $t = t_{ig}$ (point D). In this stage, the *spark-ignited flame kernel* expands outwardly, and the largest flame radius is observed at D. Due to the spark effects, the HRR at the kernel is high before 0.2 ms, see point D_1 in Fig. 5(b). Meanwhile, the heat and mass exchanges between gas and liquid phases are intensified in this stage, see from Fig. 5(c) and (d). Afterwards, the HRR pronouncedly decreases, due to considerable evaporative heat loss (Fig. 5c) and increased flame ER. This may result from high droplet loading, confirmed by the local high droplet volume fractions, still around 70% of the initial value, when the spark-ignited kernel reaches D_1 (see the detailed profiles in Fig. S5b in the Supplemental Material). After D_1, the fuel mass fraction Y_F in the pre-flame zone ($r > R_f$) gradually increases to a considerable value (> 0.08) and forms a region rich in fuel vapor, which is seen in Fig. 5(a). This is due to decreased consumption rate of fuel vapor with weakened chemical reactions. The foregoing phenomenon is associated with full dispersion of evaporating ethanol droplets in the entire burned area (i.e., $R_c = 0$) until point D_2 ($t = 0.35$ ms). At D_2, the droplets around the spark are fully vaporized, and an ECF (black line in Fig. 5) appears and moves outwardly but still behind the flame front, indicating an instantaneous HT flame. Due to the weakened chemical reactions from point D_1 to D, the maximum Y_F increases from 0.03 (Fig. 6a) to 0.0825 (Fig. 6b). This is consistent with the Y_F contours shown in Fig. 5(a). Moreover, the effective ER in the post-flame zone also increases from D_1 to D.

After the spark is terminated at D, the kernel shrinks towards E, and this is stage II. In this stage, decaying of the spark-ignited kernel is caused by strong evaporative heat loss. Meanwhile, the flame kernel transits from HT to HM state (i.e., the mixture composition at the FF changes) after point D_3 ($t = 0.55$ ms). Moreover, the ECF decelerates, which is particularly evident as the ECF is not moving around $r = 0.1$ cm in Fig. 5 after D_3. This is because the droplet evaporation slows down, due to weakened kernel and reduced heat diffusion from the flame with increased front distance. This is further demonstrated by the distributions of energy and mass transfer terms after D_3, see in Fig. 5(c) and 5(d). Nonetheless, the droplets continue vaporizing from D to E, leading to a continuous accumulation of the fuel vapor, transported to the decaying kernel (hence the latter survives). This is evident from the elevated fuel vapor mass fraction Y_F from point D (Fig. 6b) to E (Fig. 6c) near the dying kernel, e.g., $r < 0.08$ cm. Meanwhile, the oxidizer also diffuses inwardly, when comparing the Y_O distributions in Fig. 6(b) and (c) near the kernel. This also leads to decrease of the effective ER (D → E) e.g., $r < 0.08$ cm, due to dilution of fuel vapor from increased Y_O.

The kernel is initiated again at E, and beyond that, a new *re-ignited kernel* is formed and expands outwardly. This is the re-

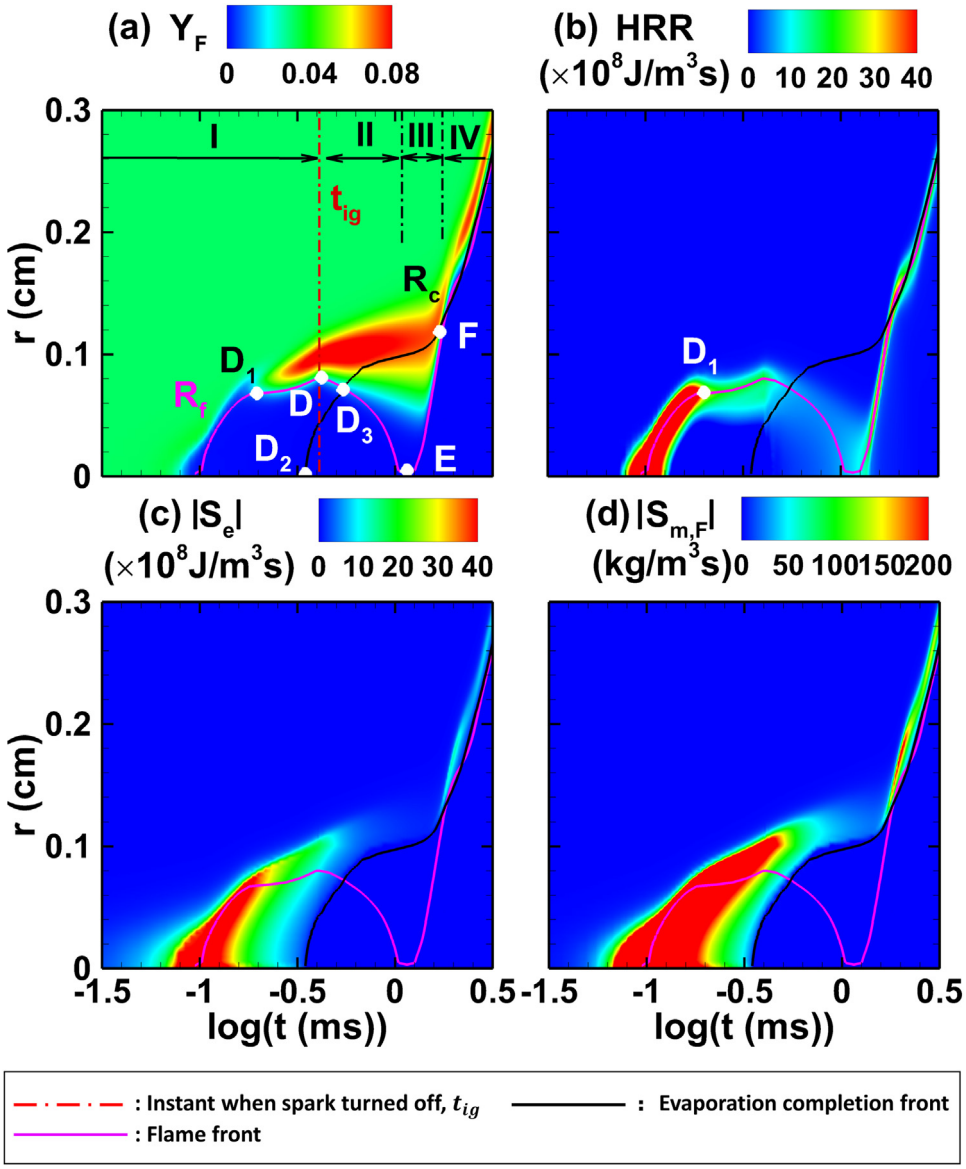

Fig. 5. $r-t$ diagrams of (a) fuel vapor mass fraction, (b) heat release rate, (c) magnitude of energy transfer term and (d) mass transfer term with $\phi_g = 0.3$, $\phi_l = 1.7$, and $d_0 = 15$ μm. $E_{ig} = 1.76$ mJ.

ignition stage (from E to F, stage III). In this stage, the FF propagates at a faster speed than the ECF. Moreover, the chemical reactions at the re-ignited kernel are strengthened. At point F, the flame ER is the smallest compared to the effective ER at other locations in Fig. 6(d). Since F, the ECF and re-ignited kernel couple again with a smaller front distance. This stage corresponds to stage IV, i.e., flame propagation in fuel sprays.

To further interpret the effects of fuel sprays on the re-ignition transient, the flame trajectories of case 2 and two gaseous flames (ER = 0.3 and 2.0, respectively correspond to ϕ_g and ϕ_{ov} of case 2) are compared in Fig. 7(a). The respective flame ERs are presented in Fig. 7(b). The ignition energies of two gaseous flames are the MIE of case 2. In Fig. 7(a), failed and successful ignition events are respectively observed for gaseous flames with the ER of 0.3 and 2.0. It is not surprising to see ignition failure when the ER is 0.3, because the flame ERs are well below the LFL. Moreover, addition of fuel droplets is beneficial in enriching the lean background gas, which can be found in case 2 in Fig. 7(b). Compared to gaseous flame with $\phi_g = 2.0$, the flame ER of case 2 is even higher around point D, which is about 2.5, close to the upper flammability limit of ethanol (around 2.9 [56]). This is because the fuel vapor from droplet evaporation considerably affects the flame ER for the HT spray flame. The higher flame ER around D leads to lower ignitability compared to the gaseous flame with $\phi_g = 2.0$.

4.2.2. Fuel-rich background gas ($\phi_g > 1.0$)

The spray flame kernel development in fuel-rich background gas will be discussed in this section and the case is parameterized by $\phi_g = 1.1$, $\phi_l = 0.9$, and $d_0 = 5$ μm (termed as case 3 hereafter) when $E_{ig} = E_{min} = 0.585$ mJ. Figure 8(a) shows the r-t diagram of fuel vapor mass fraction. Likewise, the flame trajectories and flame ER of two gaseous flames (ER = 1.1 and 2.0) with the same E_{ig} are shown in Fig. 8(b) and 8(c), respectively.

It is seen from Fig. 8(a) that the flame kernel development differs from cases 1 and 2 due to the near-stoichiometric gas ER (1.1) and fine droplets (5 μm). Meanwhile, the igniting kernel always grows in the HM mixture, although the front distance decreases with time. Compared to the ER = 1.1 gaseous flame, addition of fuel sprays delays the formation of igniting kernel and leads to lower flame propagation speed. This indicates that for the fuel-rich

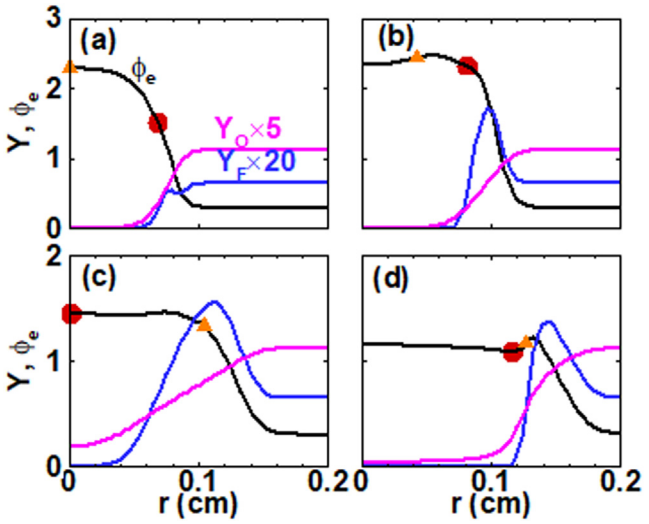

Fig. 6. Spatial distributions of fuel / oxidizer mass fractions and effective equivalence ratio at (a) D_1, (b) D, (c) E, and (d) F. Triangle: evaporation completion front. Circle: flame front.

background gas, dispersed droplets near the spark deteriorate the ignitibility of the local mixture due to evaporative heat loss and/or richer flame ER from droplet evaporation [58,59], as also seen in Fig. 8(c). Moreover, the MIE of case 3 cannot ignite the gas mixture with ER = 2.0.

Likewise, for case 4 (ϕ_g = 1.1, ϕ_l = 0.9, and d_0 = 15 μm), the $r-t$ diagram of fuel vapor mass fraction is shown in Fig. 9(a) when $E_{ig} = E_{min}$ = 1.16 mJ. The comparisons with two gaseous cases are given in Fig. 9(b) and (c) for kernel trajectories and flame ER, respectively. From Fig. 9(a), the coarse droplets (15 μm) induce the re-ignition phenomenon, which is similar to case 2. It is seen from Fig. 9(b) and 9(c) that the difference between case 4 and the gaseous flame with ER = 1.1 is identical to that for case 3. Furthermore, a richer flame ER around the re-ignited point of case 4 is observed compared to gaseous flame with ER = 2.0. Therefore, case 4 is more difficult to be ignited than the ER = 2.0 gaseous flame, consistent with the observations from case 2.

When comparing case 2 and case 4 together, the flame kernel dynamics are found to be correlated to the gas ER. For instance, it is seen that re-ignition occurs in both fuel-lean and fuel-rich background gas. Nonetheless, the extinction dynamics (e.g., the inward displacement of the FF) in two cases are different, because the flame ER is affected by gas ER. This is not reported from our previous study, i.e., Ref. [10], when $\phi_g = 0$.

For fuel-rich background gas in this section (cases 2 – 4), it should be noted that the ignition energy also affects the evolutions of front distance (ΔR) and flame ER, particularly at the early stage of the ignition event (see details in Figs. S6–S8 in the supplemental material). For instance, larger ignition energy E_{ig} leads to a larger flame radius when the ECF starts to deviate from the spark location in cases 2 and 4. This is reasonable because the embryonic kernel expands faster with a larger E_{ig}. Moreover, the flame ER is also increased due to a stronger flame kernel induced by a larger E_{ig} in cases 2 – 4. This is attributed to the intensified evaporation process from increased spark ignition E_{ig}. Meanwhile, the front distance is decreased with increased ignition energy in the kernel period. However, when the spark effects fade, the flame ER and front distance are almost not affected by the initial ignition deposition. This is similar to the findings from Fig. 4 for spray flame in the fuel-lean background gas.

4.3. Relations between flame kernel dynamics and minimum ignition energy

In this section, we will investigate the minimum ignition energy of partially pre-vaporized ethanol sprays under different background gas ERs and droplet diameters. Figure 10(a)–(f) show the change of the MIE with overall ER. Six gas ERs are considered, i.e., ϕ_g = 0.3, 0.5, 0.7, 1.1, 1.5 and 2.0, respectively. Each plot shows the results with two droplet diameters, i.e., d_0 = 5 and 15 μm. In this study, the MIE is determined from trial-and-error simulations, with errors less than 2%.

For fuel sprays in fuel-lean background gas, i.e., ϕ_g = 0.3, 0.5 and 0.7 in Fig. 10(a)–(c), the MIE firstly decreases with overall ER ϕ_{ov}. For instance, in Fig. 10(a), the MIE of the d_0 = 5 μm sprays decreases from 5.7 mJ to 0.585 mJ when ϕ_{ov} increases from 1.2 to 1.7. Case 1 (marked in Fig. 10b) with the QSSF, from Section 4.1, is from this range. As mentioned above, insufficient fuel vapor at the FF causes the QSSF. Increased ϕ_{ov} (hence ϕ_l, due to fixed ϕ_g) corresponds to a richer mixture at the FF. Therefore, the MIE decreases with increased ϕ_{ov} (ϕ_l) in this range. This is regime A. As discussed previously in case 1, the critical flame ER is lower or close to the LFL in this regime. Furthermore, the droplet diameter and pre-vaporization degree (i.e., ϕ_g) are found to affect the range of this regime. In Fig. 10(a), this regime moves leftward (smaller ϕ_{ov}) with increased droplet diameter. This can be justified by the fact that the front distance between the droplet evaporation zone and FF decreases with droplet diameter due to slower evaporation. Therefore, the local ER at the flame kernel is greater than the

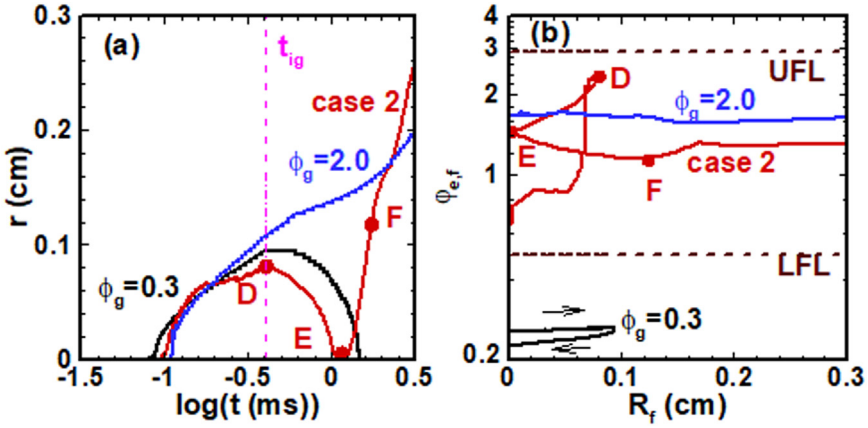

Fig. 7. (a) Flame trajectories and (b) flame ER of case 2 and two gaseous flames with ϕ_g = 0.3 and 2.0. E_{ig} = 1.76 mJ. UFL: upper flammability limit.

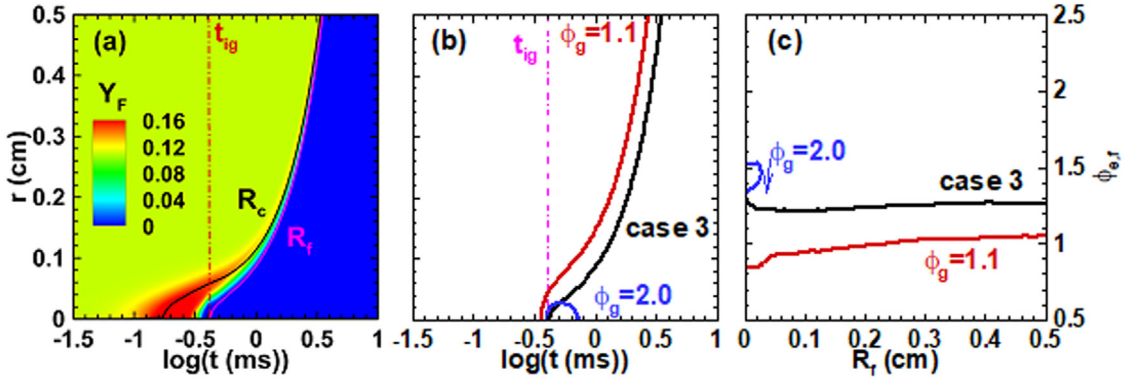

Fig. 8. (a) $r-t$ diagram of fuel vapor mass fraction with ϕ_g = 1.1, ϕ_l = 0.9, and d_0 = 5 μm (case 3). (b) Flame trajectories and (c) flame ER in case 3 and two gaseous flames with ER = 1.1 and 2.0. E_{ig} = 0.585 mJ.

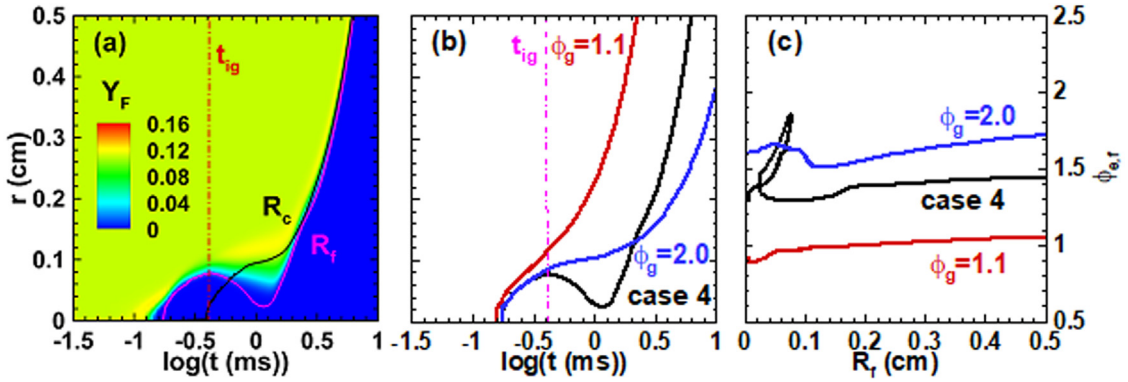

Fig. 9. (a) $r-t$ diagram of fuel vapor mass fraction with ϕ_g = 1.1, ϕ_l = 0.9, and d_0 = 15 μm (case 4). (b) Flame trajectories and (c) flame ER in case 4 and two gaseous flames with ER = 1.1 and 2.0. E_{ig} = 1.16 mJ.

unity for larger droplets under the same ϕ_{ov} or ϕ_g. Meanwhile, increased background gas ER also leads to a leftward shift of regime A in the ϕ_{ov} range if one compares Figs. 10(b) and 10(c) with Fig. 10(a). This is particularly pronounced for d_0 = 5 μm: ϕ_{ov} for regime A in Fig. 10(c) corresponds to 0.7 – 1.0, smaller than that in Fig. 10(a).

Beyond regime A, further increasing ϕ_{ov}, e.g., 1.7–3.0 in Fig. 10(a) for d_0 = 5 μm, leads to weak dependence of the MIE on overall ER (around 0.58 mJ). Compared to regime A, the fuel vapor at the FF becomes relatively sufficient due to the larger $\phi_{ov}(\phi_l)$ in this range. Meanwhile, the evaporative heat loss in this range is negligible compared to the heat released from the intensified chemical reactions. This regime is featured by a plateau value of MIE for the gaseous ethanol flame when gas ER is from 0.8 to 1.8 (see Fig. S4 in the Supplemental Material), where the overall ER slightly affects the MIE. This range of ϕ_{ov} corresponds to regime B. For fixed ϕ_g (d_0), this regime lies in a smaller ϕ_{ov} range with increased d_0 (ϕ_g), e.g., when comparing d_0 = 5 and 15 μm in Fig. 10(a) and d_0 = 5 μm in Fig. 10(a)–(c).

When $\phi_{ov} \geq$ 3.5 and d_0 = 5 μm in Fig. 10(a), the slope of the MIE–ϕ_{ov} curve is larger compared to regime B, which can be called as regime C. This results from increased flame ER (above unity, hence richer) or evaporative heat loss. Regime C with different droplet sizes is essentially induced by different mechanisms, i.e., increased flame ER for d_0 = 5μm, whereas increased evaporative heat loss for d_0 = 15 μm. Moreover, the dependence of MIE on ϕ_{ov} is stronger than that of the 5 μm droplets due to greater evaporative heat loss near the kernel. This is evident from the larger slope of regime C for fixed ϕ_g, i.e., d_0 = 5 μm and 15 μm in Fig. 10(a). Note that case 2 in Section 4.2.1 is from this regime, in which the kernel dying/re-ignition event is observed. Similarly, distribution of the two regimes in ϕ_{ov} space is also affected by the droplet diameter and background gas ER, but in a more complicated way. Explanations will be given through the regime map in Fig. 11 in a wider parameter range.

For fuel-rich gas mixtures, e.g., ϕ_g = 1.1 and 1.5 in Fig. 10(d) and (e), the MIE monotonically increases with ϕ_{ov} from the gas flame point ($\phi_{ov} = \phi_g$). Regime A is not observed due to the rich background gas. In general, the MIE variations in these regimes and the underpinning mechanisms are similar to those in the fuel-lean results. Cases 3 and 4 in Section 4.2.2 can be categorized into regimes B and C, respectively (marked in Fig. 10d). It is seen that the re-ignition phenomenon also occurs in regime C (case 4) of the fuel-rich background gas. With further increased gas ER above unity, i.e., ϕ_g = 2.0 in Fig. 10(f), regime B also disappears or gets shortened compared to Fig. 10(d) and 10(e). This is because the background gas under ϕ_g = 2.0 is more difficult to be ignited than that with gas ER < 2.0 (see Fig. S4 from Supplemental Material). Therefore, only regime C is presented in Fig. 10(f).

The relations between the flame kernel dynamics and MIE are further summarized in Table 1. As mentioned in Refs. [2,10,27,60,61], the MIE dependence on the overall ER are *U*-shaped, and there exists an optimal equivalence ratio. This is consistent with the results presented in Fig. 10(a)–(c) for partially prevaporized spray flames with fuel-lean background gas. Specifically, regime A(C) from Fig. 10 and Table 1 corresponds to the left (right) branch of the *U*-shaped MIE curves in Refs. [2,10,27,60,61]. Meanwhile, regime B is equivalent to the range of optimal ER in those studies. However, they do not correlate the unsteady kernel dynamics to these regimes. Moreover, as for MIE shown in Fig. 10(d)–(f), limited results have been reported from previous studies, due to the relatively rich gas phase.

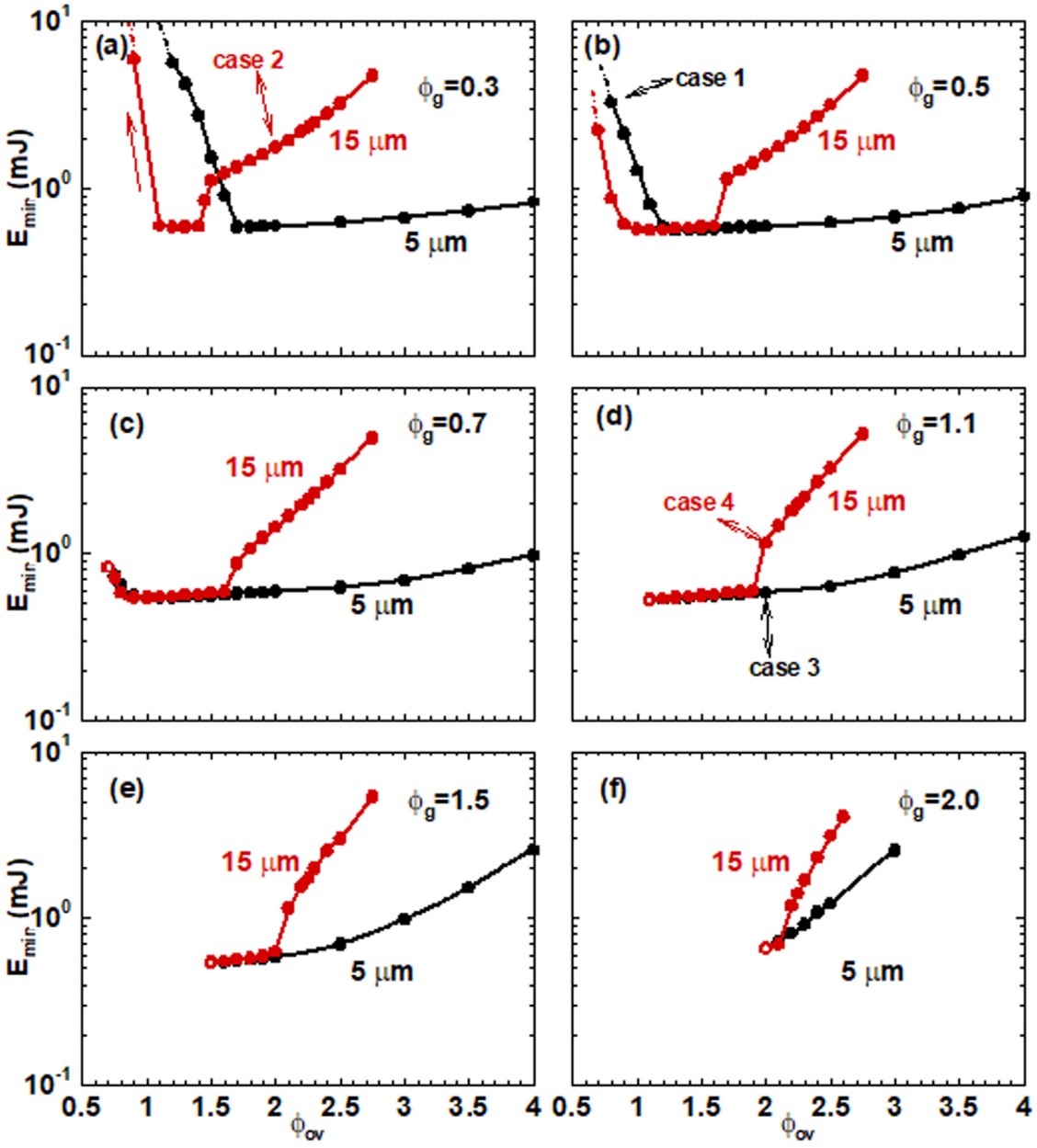

Fig. 10. Minimum ignition energy as a function of overall ER with different background gas ERs: (a) ϕ_g = 0.3, (b) ϕ_g = 0.5, (c) ϕ_g = 0.7, (d) ϕ_g = 1.1, (e) ϕ_g = 1.5, (f) ϕ_g = 2.0. Hollow symbol: gaseous flame under the corresponding background gas ER, i.e., $\phi_{ov} = \phi_g$.

Table 1
Summary of regimes A–C of the MIE variation.

Regime	MIE variation	Key phenomena when the ignition energy is MIE	Justification
A	Decrease with ϕ_{ov}	Quasi-stationary spherical flame	Flame ER near LFL
B	Weak dependence on ϕ_{ov}	Kernel formation and continuous growth	Appropriate flame ER, negligible evaporative heat loss
C	Increase with ϕ_{ov}	*Re*-ignition with large droplets	Flame ER above unity, considerable evaporative heat loss

To generalize the regimes of spray flame ignition, Fig. 11 summarizes three regimes of spray flame ignition in ϕ_g-ϕ_{ov} space based on the MIE variation and different flame kernel dynamics. A lower ignitability limit (dash-dotted lines) is achieved, below which the mixture is not ignitable, i.e., the blue shaded zone, with the current spark radius (400 μm) and duration (400 μm) used in our simulations. Note that these spark parameters may affect this limit, but it will not be expanded for discussion in this paper. In Fig. 11, it is seen that this limit decreases with increased ϕ_g. This is because the flame ER is increased with increased ϕ_g when the ϕ_{ov} is fixed. Moreover, increased droplet diameter from 5 to 15 μm leads to a smaller lower ignitability limit due to increased flame ER under the same gas ER. Further increasing the background gas ER, i.e., $\geq$ 0.7 in Fig. 11(a) and (b), this ignitability limit disappears. This is reasonable because the background gas ER is generally above the LFL (around 0.5 for ethanol) in these cases. Instead, the lower boundary to achieve ignition success with a proper ignition energy is replaced by the condition of $\phi_g = \phi_{ov}$ (i.e., gaseous

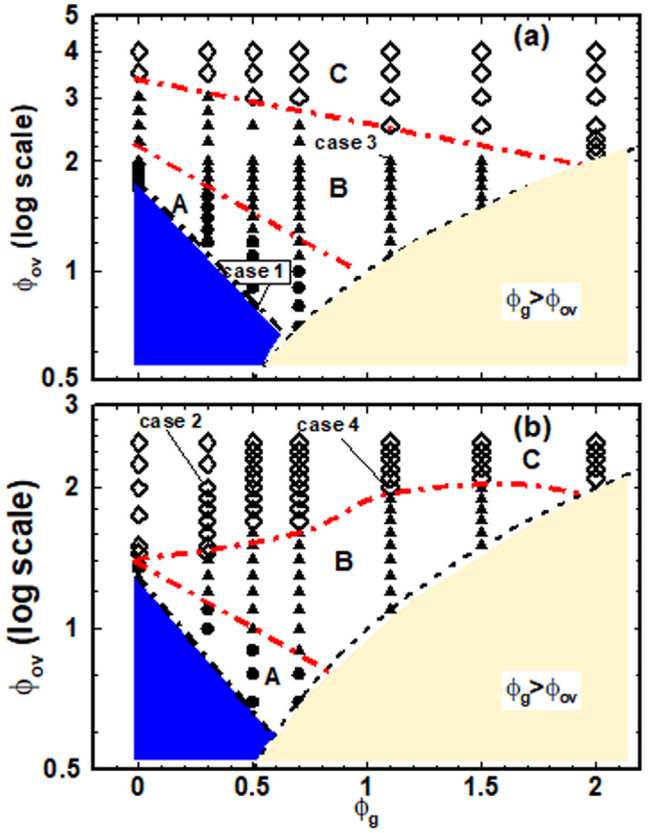

Fig. 11. Regime map of ethanol spray ignition regime in $\phi_g - \phi_{ov}$ space: (a) $d_0 = 5$ μm and (b) $d_0 = 15$ μm. Red dash-dotted line: regime boundary. Black dashed line: $\phi_g = \phi_{ov}$. Black dash-dotted line: ignitability limit of ethanol sprays.

flame), below which is the yellow area with $\phi_g > \phi_{ov}$ (physically unachievable).

In Fig. 11(a) ($d_0 = 5$ μm), the overall ER ϕ_{ov} of the boundary between regime A(B) and B(C) decreases with background gas ER ϕ_g. This is because the flame ER is the controlling parameter in the kernel dynamics and MIE variations of spray flame with small droplet diameter. Meanwhile, for fixed ϕ_{ov}, the flame ER decreases with decreased gas ER. Similarly, when $d_0 = 15$ μm in Fig. 11(b), the ϕ_{ov} of the A-B regime boundary also decreases with the gas ER. On the contrary, that of the B-C regime boundary increases with the gas ER. This is because the key factor (evaporative heat loss) is weakened with increased gas ER when ϕ_{ov} is fixed. Nonetheless, the B-C regime boundary in both Fig. 11(a) and (b) intersect with $\phi_g = \phi_{ov}$ before $\phi_g = 2.0$. This justifies why only regime C is observed at relatively large gas ER, e.g., in Fig. 10(f).

Compared to Ref. [10], one can see that the analysis in this section furthers the study on effect of background gas ER (ϕ_g) and its correlation with the MIE and flame kernel dynamics. The dependence of different regimes (A, B, and C) on varied gas ER from fuel-lean to fuel-rich conditions are revealed based on Figs. 10 and 11. A comprehensive understanding of spray flame kernel dynamics is hence obtained. Moreover, the above regime categorizations may be extended to other fuels because the flame ER variation with gas ER and liquid properties can be generalized, although the lower and upper flammability limits are fuel-dependent [56].

5. Conclusion

This study numerically investigates spark ignition of ethanol droplet/vapor/air mixtures with a Eulerian-Eulerian method and detailed chemical mechanism. Different droplet sizes and gas/overall equivalence ratios are considered. The evaporation completion front is introduced to study the flame-droplet interaction. The gas composition at the flame front is quantified by the flame equivalence ratio.

For overall fuel-lean two-phase mixtures, the quasi-stationary spherical flame occurs due to low flame ER, which is around the lower flammability limit. The QSSF is terminated when the front distance is the largest due to the continuous fuel vapor diffusion from the evaporation zone to the flame front. Moreover, for overall fuel-rich mixtures, re-ignition of the sprays proceeds when the droplet diameter is 15 μm for fuel sprays in both lean and rich background gas. This is caused by the rich gas composition and/or considerable evaporative heat loss.

Through the comparisons with gaseous flames with gas/overall equivalence ratio, existence of fuel droplets affects flame kernel behavior and ignitability due to the heat and mass transfer between two phases. Moreover, the flame ER increases with ignition energy due to the intensified evaporation process. Meanwhile, the front distance between the flame front and evaporation completion front decreases with ignition energy. However, when the flame radius is sufficiently large, the ignition energy effects are negligible.

The minimum ignition energies of ethanol spray flames are investigated, considering different gas and overall ERs. Three regimes (A, B and C) are identified based on different dependence of the MIE on the overall ER. Different igniting kernel dynamics of these regimes are summarized. In regime A (C), the MIE decreases (increases) with increased overall ER for fixed gas ER. As for regime B, the MIE shows weak dependence on overall ER. Moreover, it is found that regime A is featured by the QSSF phenomenon, whilst regime C is correlated to the extinction/re-ignition events with large droplet size. The evolution of the three regimes with varied gas and overall ERs are compiled in parameter space of overall and gas ERs. For increased gas ER, the lower ignitibility limit decreases. With increased gas ER from fuel-lean side, regime A disappears when gas ER is close to stoichiometry. Furthermore, regime B only appears with a narrow range of overall ER when gas ER is above unity. When the background gas ER is high (i.e., higher than 2.0), only regime C exists.

Declaration of Competing Interest

None.

Acknowledgment

The calculations are performed with the ASPIRE 1 Cluster from National Supercomputing Center in Singapore (https://www.nscc.sg/). QL is supported by NUS Research Scholarship. The work is supported by MOE Tier 1 grant (A-0005238-01-00).

Supplementary materials

Supplementary material associated with this article can be found, in the online version, at doi:10.1016/j.combustflame.2023.112622.

References

[1] E. Mastorakos, Forced ignition of turbulent spray flames, Proc. Combust. Inst. 36 (2017) 2367–2383.
[2] S.K. Aggarwal, A review of spray ignition phenomena: present status and future research, Prog. Energy Combust. Sci. 24 (1998) 565–600.
[3] E. Mastorakos, Ignition of turbulent non-premixed flames, Prog. Energy Combust. Sci. 35 (2009) 57–97.
[4] Y. Mizutani, K. Nakabe, M. Fuchihata, F. Akamatsu, M. Zaizen, S.H. El-Emam, Spark-ignited spherical flames propagating in a suspended droplet cloud, At. Sprays 3 (1993).

[5] F. Akamatsu, K. Nakabe, M. Katsuki, Y. Mizutani, T. Tabata, Structure of spark-ignited spherical flames propagating in a droplet cloud, Developments in Laser Techniques and Applications to Fluid Mechanics, Springer (1996), pp. 212–223.
[6] L. Fan, B. Tian, C.T. Chong, M.N.M. Jaafar, K. Tanno, D. McGrath, P.M. de Oliveira, B. Rogg, S. Hochgreb, The effect of fine droplets on laminar propagation speed of a strained acetone-methane flame: experiment and simulations, Combust. Flame 229 (2021) 111377.
[7] A. Neophytou, E. Mastorakos, R.S. Cant, DNS of spark ignition and edge flame propagation in turbulent droplet-laden mixing layers, Combust. Flame 157 (2010) 1071–1086.
[8] G. Ozel Erol, J. Hasslberger, M. Klein, N. Chakraborty, A direct numerical simulation analysis of spherically expanding turbulent flames in fuel droplet-mists for an overall equivalence ratio of unity, Phys. Fluids 30 (2018) 86104.
[9] P.M. de Oliveira, E. Mastorakos, Mechanisms of flame propagation in jet fuel sprays as revealed by OH/fuel planar laser-induced fluorescence and OH* chemiluminescence, Combust. Flame 206 (2019) 308–321.
[10] Q. Li, H. Zhang, Forced ignition and oscillating flame propagation in fine ethanol sprays, Proc. Combust. Inst. (2022) in press, doi:10.1016/j.proci.2022.07.125.
[11] Y. Zhuang, H. Zhang, Effects of water droplet evaporation on initiation, propagation and extinction of premixed spherical flames, Int. J. Multiph. Flow 117 (2019) 114–129.
[12] Y. Zhuang, H. Zhang, On flame bifurcation and multiplicity in consistently propagating spherical flame and droplet evaporation fronts, Int. J. Multiph. Flow (2020) 103220.
[13] Q. Li, H. Zhang, C. Shu, Propagation of weakly stretched premixed spherical spray flames in localized homogeneous and heterogeneous reactants, Phys. Fluids 32 (2020) 123302.
[14] Q. Li, C. Shu, H. Zhang, On the evolution of fuel droplet evaporation zone and its interaction with flame front in ignition of spray flames, Combust. Theory Model. (2021), doi:10.1080/13647830.2021.2002416.
[15] F. Atzler, F.X. Demoulin, M. Lawes, Y. Lee, N. Marquez, Burning rates and flame oscillations in globally homogeneous two-phase mixtures (flame speed oscillations in droplet cloud flames), Combust. Sci. Technol. 178 (2006) 2177–2198.
[16] S.A. Sulaiman, Burning Rates and Instabilities in the Combustion of Droplet and Vapour Mixtures, The University of Leeds, Leeds, U.K., 2006.
[17] F. Atzler, M. Lawes, S.A. Sulaiman, R. Woolley, Effects of droplets on the flame speed of laminar Iso-octane and air aerosols, Proceedings of the 10th International Conference on Liquid Atomization and Spray Systems (2006).
[18] D. McGrath, L. Fan, S. Gkantonas, S. Hochgreb, The effect of fuel droplets on the burning velocity of strained laminar acetone/air flames, Proc. Combust. Inst. (2022) In Press.
[19] P.M. de Oliveira, P.M. Allison, E. Mastorakos, Ignition of uniform droplet-laden weakly turbulent flows following a laser spark, Combust. Flame 199 (2019) 387–400.
[20] R. Thimothée, C. Chauveau, F. Halter, I. Gökalp, Experimental investigation of the passage of fuel droplets through a spherical two-phase flame, Proc. Combust. Inst. 36 (2017) 2549–2557.
[21] H.N.S. Rao, A.H. Lefebvre, Ignition of kerosine fuel sprays in a flowing air stream, Combust. Sci. Technol. 8 (1973) 95–100.
[22] K.V.L. Rao, A.H. Lefebvre, Minimum ignition energies in flowing kerosine-air mixtures, Combust. Flame 27 (1976) 1–20.
[23] D.R. Ballal, A.H. Lefebvre, Ignition of liquid fuel sprays at subatmospheric pressures, Combust. Flame 31 (1978) 115–126.
[24] D.R. Ballal, A.H. Lefebvre, Ignition and flame quenching of quiescent fuel mists, Proc. R. Soc. London. A. Math. Phys. Sci. 364 (1978) 277–294.
[25] D.R. Ballal, A.H. Lefebvre, Ignition and flame quenching of flowing heterogeneous fuel-air mixtures, Combust. Flame 35 (1979) 155–168.
[26] A.M. Danis, I. Namer, N.P. Cernansky, Droplet size and equivalence ratio effects on spark ignition of monodisperse n-heptane and methanol sprays, Combust. Flame 74 (1988) 285–294.
[27] A.K. Singh, C.E. Polymeropoulos, Spark ignition of aerosols, Symp. (Int.) Combust. 21 (1988) 513–519.
[28] S.K. Aggarwal, W.A. Sirignano, Ignition of fuel sprays: deterministic calculations for idealized droplet arrays, Symp. (Int.) Combust. 20 (1985) 1773–1780.
[29] S.K. Aggarwal, W.A. Sirignano, Ignition of Polydisperse Sprays: importance of D20, Combust. Sci. Technol. 46 (1986) 289–300.
[30] S.K. Aggarwal, Ignition and flame propagation in dilute polydisperse sprays-Importance of d32 and d20, J. Propuls. Power. 4 (1988) 14–21.
[31] D.R. Ballal, A.H. Lefebvre, A general model of spark ignition for gaseous and liquid fuel-air mixtures, Symp. (Int.) Combust. 18 (1981) 1737–1746.
[32] W. Han, Z. Chen, Effects of finite-rate droplet evaporation on the ignition and propagation of premixed spherical spray flame, Combust. Flame. 162 (2015) 2128–2139.
[33] Z. Chen, Studies on the Initiation, Propagation, and Extinction of Premixed Flames, Princeton University, NJ, USA, 2009.
[34] Z. Yu, H. Zhang, Reaction front development from ignition spots in n-heptane/air mixtures: low-temperature chemistry effects induced by ultrafine water droplet evaporation, Phys. Fluids 33 (2021) 83312.
[35] Z. Chen, M.P. Burke, Y. Ju, On the critical flame radius and minimum ignition energy for spherical flame initiation, Proc. Combust. Inst. 33 (2011) 1219–1226.
[36] R. Blouquin, G. Joulin, On the quenching of premixed flames by water sprays: influences of radiation and polydispersity, Symp. (Int.) Combust. 27 (1998) 2829–2837.
[37] N.S. Belyakov, V.I. Babushok, S.S. Minaev, Influence of water mist on propagation and suppression of laminar premixed flame, Combust. Theory Model. 22 (2018) 394–409.
[38] B. Abramzon, W.A. Sirignano, Droplet vaporization model for spray combustion calculations, Int. J. Heat Mass Transf. 32 (1989) 1605–1618.
[39] D.W. Green, M.Z. Southard, Perry's Chemical Engineers' Handbook, McGraw-Hill Education, 2019.
[40] E.N. Fuller, P.D. Schettler, J.C. Giddings, New method for prediction of binary gas-phase diffusion coefficients, Ind. Eng. Chem. 58 (1966) 18–27.
[41] E.L. Cussler, E.L. Cussler, Diffusion: Mass Transfer in Fluid Systems, Cambridge University Press, 2009.
[42] L. Schiller, A. Naumann, A drag coefficient correlation, Z. Vereins Dtsch. Ingenieure 77 (1935) 318–320.
[43] B.E. Poling, J.M. Prausnittz, J.P. O'Connell, The Properties of Gases and Liquids, 5th Edition, McGraw-Hill Education, 2001.
[44] J.W.E. Ranz, W.R. Marshall, Vaporation from drops, part I, Chem. Eng. Prog. 48 (1952) 141–146.
[45] B. Van Leer, On the relation between the upwind-differencing schemes of Godunov, Engquist–Osher and Roe, SIAM J. Sci. Stat. Comput. 5 (1984) 1–20.
[46] N.M. Marinov, A detailed chemical kinetic model for high temperature ethanol oxidation, Int. J. Chem. Kinet. 31 (1999) 183–220.
[47] L. Ma, D. Roekaerts, Numerical study of the multi-flame structure in spray combustion, Proc. Combust. Inst. 36 (2017) 2603–2613.
[48] A. Giusti, E. Mastorakos, Detailed chemistry LES/CMC simulation of a swirling ethanol spray flame approaching blow-off, Proc. Combust. Inst. 36 (2017) 2625–2632.
[49] M. Chrigui, A.R. Masri, A. Sadiki, J. Janicka, Large eddy simulation of a polydisperse ethanol spray flame, Flow, Turbul. Combust. 90 (2013) 813–832.
[50] D. Bradley, M. Lawes, S. Liao, A. Saat, Laminar mass burning and entrainment velocities and flame instabilities of i-octane, ethanol and hydrous ethanol/air aerosols, Combust. Flame 161 (2014) 1620–1632.
[51] A. Frendi, M. Sibulkin, Dependence of Minimum Ignition Energy on Ignition Parameters, Combust. Sci. Technol. 73 (1990) 395–413.
[52] H. Zhang, Z. Chen, Spherical flame initiation and propagation with thermally sensitive intermediate kinetics, Combust. Flame 158 (2011).
[53] Y. Wang, W. Han, Z. Chen, Effects of fuel stratification on ignition kernel development and minimum ignition energy of n-decane/air mixtures, Proc. Combust. Inst. 37 (2019) 1623–1630.
[54] A. Neophytou, E. Mastorakos, Simulations of laminar flame propagation in droplet mists, Combust. Flame 156 (2009) 1627–1640.
[55] A.P. Da Cruz, A.M. Dean, J.M. Grenda, A numerical study of the laminar flame speed of stratified methane/air flames, Proc. Combust. Inst. 28 (2000) 1925–1932.
[56] I. Glassman, R.A. Yetter, N.G. Glumac, Combustion, Academic Press, 2014.
[57] Q. Li, H. Zhang, Ignition of premixed spherical spray flames, Proceedings of the 15th International Conference on Liquid Atomization and Spray Systems (2021).
[58] A.P. Wandel, N. Chakraborty, E. Mastorakos, Direct numerical simulations of turbulent flame expansion in fine sprays, Proc. Combust. Inst. 32 (2009) 2283–2290.
[59] A.P. Wandel, Influence of scalar dissipation on flame success in turbulent sprays with spark ignition, Combust. Flame 161 (2014) 2579–2600.
[60] S.K. Aggarwal, I. Nguyen, Ignition behavior of a fuel spray flowing in a tube, Chem. Eng. Commun. 88 (1990) 23–29.
[61] C.B. Graves, Y.L. Tang, J.G. Skifstad, Ignition of a Fuel Spray By a Hot Surface, AIAA Pap. I (1985) 1994–2001.